Comparisons of IMERG Version 06 Precipitation At and Between Passive Microwave Overpasses in the Tropics

Manikandan Rajagopal,[a] Edward Zipser,[a] George Huffman,[b] James Russell,[a] Jackson Tan [b, c]

[a] *University of Utah, Salt Lake City, Utah*

[b] *NASA Goddard Space Flight Center, Greenbelt, Maryland*

[c] *Universities Space Research Association, Columbia, Maryland*

Corresponding author: Manikandan Rajagopal, mani.rajagopal@utah.edu

File generated with AMS Word template 1.0

ABSTRACT

The Integrated Multi-Satellite Retrievals for Global Precipitation Measurement Mission (IMERG) is a global precipitation product that uses precipitation retrievals from the virtual constellation of satellites with passive microwave (PMW) sensors, as available. In the absence of PMW observations, IMERG uses a Kalman filter scheme to morph precipitation from one PMW observation to the next. In this study, an analysis of convective systems observed during the Convective Process Experiment (CPEX) suggests that IMERG precipitation depends more strongly on the availability of PMW observations than previously suspected. Following this evidence, we explore systematic biases in IMERG through bulk statistics.

In two CPEX case studies, cloud photographs, pilot's radar, and infrared imagery suggest that IMERG represents the spatial extent of precipitation relatively well when there is a PMW observation but sometimes produces spurious precipitation areas in the absence of PMW observations. Also, considering an observed convective system as a precipitation object in IMERG, the maximum rain rate peaked during PMW overpasses, with lower values between them. Bulk statistics reveal that these biases occur throughout IMERG Version 06. We find that locations and times without PMW observations have a higher frequency of light precipitation rates and a lower frequency of heavy precipitation rates due to retrieval artifacts. These results reveal deficiencies in the IMERG Kalman Filter scheme, which have led to the development of the Scheme for Histogram Adjustment with Ranked Precipitation Estimates in the Neighborhood (SHARPEN; described in a companion paper) that will be applied in the next version of IMERG.

1. Introduction

Precipitation has direct impacts on human populations through natural disasters (e.g., Bodenreider et al. 2019; Paul et al. 2019) and by influencing the global economy through agriculture (e.g., Zhang et al. 2012; Sohoulande et al. 2019) and commerce (Steinker et al. 2015; Verstraete et al. 2019). Satellites are crucial for observing atmospheric variables, including precipitation, over remote locations such as oceans and mountains, where surface observations are often scarce. The most detailed precipitation measurement from space is possible through the precipitation radar onboard the Tropical Rainfall Measuring Mission (TRMM; Kummerow et al. 1998) satellite and its successor, the Global Precipitation Measurement mission (GPM; Hou et al. 2014) Core Observatory satellite. The cloud radar onboard the CloudSat satellite is complementary to the precipitation radars since it is sensitive to light snow and rain (Hayden et al. 2018). These precipitation and cloud radars have extremely sparse revisit times, so long-term global satellite precipitation products use passive microwave (PMW) sensor observations. These long-term precipitation records help us understand the hydrological cycle and climate change impacts at global and regional scales. These records include satellite precipitation data such as the Global Precipitation Climatology Project (GPCP; Huffman et al. 1997; Adler et al. 2018) and the TRMM Multi-satellite Precipitation Analysis (TMPA; Huffman et al. 2007), which have regularly been used to study recent climate trends (e.g., Gu et al. 2007; Zhou et al. 2015). Despite their value in climate analyses, both GPCP and TMPA have relatively coarse time/space resolution; TMPA, for example, is available every three hours with a spatial resolution of 0.25° x 0.25° (Huffman et al. 2007). This relatively coarse temporal resolution makes TMPA less suitable for studying important objects in precipitation fields such as Mesoscale Convective Systems (MCSs), which can produce severe weather events that cause damage through strong winds,

floods, and hail (Akaeda et al. 1995; McCollum et al. 1995). Also, MCSs contribute more than 50% of annual rainfall in the tropics (Mohr et al. 1999; Nesbitt et al. 2006; Liu 2011).

The Integrated Multi-Satellite Retrievals for GPM (IMERG), the successor to TMPA, is a global precipitation product at a spatial resolution of 0.1° x 0.1°, available every 30 minutes, and is therefore more suitable to investigate MCSs and better resolve precipitation events. IMERG follows the pioneering TMPA approach, achieving near-global coverage by taking advantage of a virtual constellation (because their orbits are not coordinated) of low Earth orbit (LEO) satellites with PMW sensors. At the locations with PMW observations, IMERG uses the Goddard Profiling algorithm (GPROF2017) that converts PMW brightness temperature (T_b) to precipitation estimates for various PMW sensors (Kummerow et al. 2015; Randel et al. 2020), except the Sounder for Probing Vertical Profiles of Humidity (SAPHIR), for which the Precipitation Retrieval and Profiling Scheme (PRPS) is employed (Kidd et al. 2018b). At locations without PMW observations, IMERG uses a time morphing scheme, based on Kalman Filtering (Joyce et al. 2011), to estimate precipitation.

For both weather and climate research, it is vital to understand the strengths and limitations of IMERG precipitation. Past validation studies compared precipitation estimates for various PMW sensors to the GPM dual-frequency precipitation radar (DPR), rain gauges, or ground radar. They show that GPROF overestimates light precipitation rates and underestimates heavy precipitation rates (Tan et al. 2018; Kidd et al. 2018a; You et al. 2020). In addition to differences in estimates, they found that PMW precipitation has a higher frequency of light rain rates and a lower occurrence of heavy precipitation rates than surface observations. The higher frequency of light precipitation rates may be attributed to the Bayesian nature of the GPROF algorithm, where the observed PMW brightness temperatures are matched to the closest values in *a priori* database. For each pixel, this produces multiple

matches, i.e., multiple surface precipitation rates, including zeros. The Bayesian averaging of multiple values at each pixel results in fewer zeros and a higher frequency of light rain rates. IMERG uses GPROF precipitation after removing unreasonably low rain rates through thresholding and histogram adjustment to combined radar-radiometer precipitation. The past validation studies have evaluated GPROF precipitation estimates with observations, but there are fewer studies (Tan et al. 2016; Maranan et al. 2020) that examined IMERG precipitation estimates from the morphing algorithm, which is the focus of this work.

The studies mentioned above and many others (Sungmin et al. 2017; Sharifi et al. 2016; Asong et al. 2017; Watters et al. 2018; Bytheway et al. 2020; Tapiador et al. 2020; Gowan et al. 2020) involve point-to-point comparisons of GPROF or IMERG precipitation with other observations at different space and time resolutions. As an alternative to the point-to-point comparison, an object-based approach (e.g. Davis et al. 2006; Johnson et al. 2013) has recently been introduced for evaluating reanalyses, model forecasts, and other global gridded products. This entails identifying objects in the fields of interest and establishing biases or errors based on these objects' properties. However, object-based approaches to validating IMERG are rare. Cui et al. (2020) compared MCSs tracked in IMERG with MCSs defined using ground-based radar precipitation estimates over the continental United States from 2014 to 2016. They found that MCSs in IMERG had systematically larger precipitation areas and higher precipitation volume than radar-observed objects. To our knowledge, there have not been similar object-based approaches to the validation of IMERG algorithmic components over tropical oceans.

In this work, we use an object-based approach and the aircraft data from two case studies from the Convective Processes Experiment (CPEX) to investigate the representation of MCSs in IMERG. These MCSs represented as IMERG precipitation objects occasionally exhibit an

118 unrealistic change in precipitation area and maximum rain rate in the absence of PMW
119 observations. Since these case studies are too few to provide definitive bias characteristics,
120 we use bulk statistics to show the systematic differences between IMERG precipitation
121 estimates from the GPROF and morphing algorithms.

122 The rest of the article is structured as follows. Section 2 describes the CPEX field
123 program and the DC-8 aircraft instrumentation with the forward camera and pilot's
124 radarscope used to compare with IMERG precipitation estimates. Then, we summarize the
125 IMERG V06 Final Run procedure to estimate precipitation both during and, with greater
126 complexity, between PMW overpasses. Section 3 presents the subjective tracking of MCSs
127 and their properties inferred from IMERG for two case studies from the CPEX field program.
128 Then a method for constructing precipitation rate distributions over the tropics from 2001-
129 2019 is outlined. Results presented in Section 4 show specific differences in IMERG
130 precipitation during and between PMW overpasses, both for two case studies and bulk
131 statistics from 2001 to 2019. Section 5 discusses these findings and Section 6 summarizes the
132 conclusions.

133 ## 2. Data

134 *a. CPEX aircraft data*

135 CPEX was a National Aeronautics and Space Administration (NASA) sponsored field
136 program conducted in May-June 2017. The DC-8 aircraft carried a range of remote sensing
137 instruments to measure vertical profiles of temperature, humidity, wind, and hydrometeors to
138 study the environmental conditions and the convection. Also, the aircraft had a forward
139 camera, a nadir camera, and a pilot's radarscope that provided visual references. During its
140 100 flight hours, the DC-8 investigated MCSs over the Gulf of Mexico, the Caribbean Sea,

and the western Atlantic. The forward camera and forward-looking pilot's radar give a holistic view of each MCS and are more valuable for IMERG validation than the downward-pointing aircraft precipitation radar. This is because the aircraft precipitation radar resolution and its swath are smaller than most PMW sensor footprints, rendering their comparisons less useful. The IMERG animation overlaid with the aircraft track, position, and heading are visually compared with the forward camera and pilot's radar from multiple CPEX missions. Only the evaluation for MCSs observed on June 6th and 10th 2017, are presented here. They both highlight the differences in IMERG precipitation during and between PMW overpasses.

b. IMERG Version 06

IMERG precipitation products are available at three different latencies, namely Early Run (~ 4 hours), Late Run (~14 hours), and Final Run (~3.5 months), to cater to the time-sensitivities of different applications. In this study, we use the half-hourly precipitation from the Version 06 Final Run, which is a research-quality product. IMERG uses multiple algorithms/procedures for inter-calibration, precipitation estimates, and bias corrections. Also, there exist differences in algorithmic steps between different Runs. Since we use the half-hourly Final Run in this study, only its algorithmic components will be summarized here. Information on other Runs, daily, and monthly products are available in the technical documentation and Algorithm Theoretical Basis Document (Huffman et al. 2019a, 2019b).

IMERG uses observations from a virtual constellation of LEO satellites with PMW sensors to create near-global precipitation products. The final IMERG precipitation estimate is a multi-step process starting with the inter-calibration of T_b of various PMW sensors against the TRMM Microwave Imager (TMI) or GPM Microwave Imager (GMI), depending on available periods of coincidence. The GPROF (Version 2017) algorithm uses a Bayesian approach to convert the inter-calibrated T_b of multiple PMW frequencies of a sensor to

surface precipitation (Kummerow et al. 2015). The resulting PMW precipitation has a resolution that depends on sensor frequency channels (You et al. 2020, Table1). These GPROF precipitation estimates are regridded to a 0.1° x 0.1° spatial grid using nearest-neighbor interpolation. The constellation PMW precipitation rates are calibrated to TMI or GMI precipitation rates through climatological histogram matching. This removes most differences in "precipitation rate frequency distribution" that would otherwise contaminate the IMERG inputs. All the PMW precipitation fields are then dynamically calibrated to TRMM or GPM's Combined Radar Radiometer Algorithm (CORRA; Olson et al. 2011) precipitation, which is considered superior to individual radar or radiometer precipitation.

The available PMW observations during a 30-minute interval have only partial global coverage. In the gaps between PMW sensor swaths, IMERG uses the Kalman Filter (KF)-based time morphing scheme, adapted from the Climate Prediction Center (CPC) Morphing technique (CMORPH-KF; Joyce et al. 2004, 2011; Xie et al. 2017), to interpolate precipitation between PMW observation times. The time morphing scheme uses the Kalman Filter weighted averaging to combine precipitation estimates from three sources: (1) forward propagated precipitation from the past PMW observation, (2) backward propagated precipitation from the future PMW observation, and (3) IR precipitation from geostationary satellites at the analysis time. The motion vectors used to propagate precipitation in IMERG Version 06 (Final Run) are computed from a time sequence of the total column water vapor (TQV) fields as analyzed by the Modern-Era Retrospective analysis for Research and Applications, Version 2 (MERRA-2; Gelaro et al. 2017; Tan et al. 2019). This is a change from the earlier versions of IMERG (and CMORPH-KF) that relied on motion vectors diagnosed from geostationary IR data. The IR precipitation input to the Kalman Filter is based on the Precipitation Estimation from Remotely Sensed Information using Artificial

189 Neural Networks – Cloud Classification System (PERSIANN-CCS) algorithm. This
190 algorithm converts IR cloud-top T_b gradients into precipitation estimates using neural
191 networks, trained on coincident IR and PMW observations (Hong et al. 2004; Nguyen et al.
192 2018). IMERG computes the weighted average of all three sources (forward propagated,
193 backward propagated, and IR precipitation), using Kalman Filter weights that are
194 proportional to their respective locally estimated error-variance. The Kalman weight for
195 propagated PMW precipitation decreases with increasing propagation time since the PMW
196 observation (Joyce et al. 2011). Tan et al. (2016) and Maranan et al. (2020) defined three
197 groups in the absence of instantaneous PMW observations: "morph", "IR-only", and
198 "morph+IR", based on whether the Kalman Filter uses propagated PMW precipitation, IR
199 precipitation, or both. In this article, we follow Joyce et al. (2011) and use the alternative
200 definition for "morphing" to refer to Kalman weighted average estimates that include all three
201 groups. In other words, “morphing” here refers to output from the Kalman filter that strives to
202 produce a smooth transition from one PMW observation to the next.

203 Finally, bias corrections computed using monthly rain gauge data from the Global
204 Precipitation Climatology Center (GPCC; Schneider et al. 2014), are applied to merged
205 precipitation fields from PMW and morphing. We use these gauge calibrated precipitation
206 fields to compute bulk statistics; however, using the uncalibrated precipitation yielded similar
207 results.

208 In addition to the estimated precipitation, each half-hour data file has variables to identify
209 the source of precipitation estimates (Tan et al. 2016). The variable “HQprecipSource” has a
210 PMW sensor index value for each grid cell, including the value zero when there is no PMW
211 observation. The variable “IRkalmanFilterWeight” has Kalman weights for IR precipitation
212 expressed in percentage, and the remaining percentage is the weight assigned to propagated

PMW precipitation. In the half-hour interval immediately before and after a PMW observation, the morphing algorithm weights only the forward and backward propagated PMW precipitation. Hence, the "IRkalmanFilterWeight" is zero in such locations. More than 30 minutes away from a PMW observation, the morphing algorithm weights together forward propagated, backward propagated, and IR precipitation. The complete list of data variables, description, and index values for various PMW sensors is available in the IMERG documentation (Huffman et al. 2019a, 2019b).

3. Methods

a. MCSs: Tracking and properties

The initial focus of our analyses is two MCSs that the DC-8 aircraft investigated during the CPEX field campaign. On June 6th 2017 at 09:00 UTC, an MCS started as an isolated convective system (Fig. 1). Later, around 13:00 UTC, the system connected with the adjacent precipitation area of low rain rates (< 4 mm hr^{-1}), but the MCS remained distinct and subjectively identifiable. In the next six hours, it grew upscale to become a large and intense MCS at 19:00 UTC. At about 22:00 UTC, the system merged with a precipitation band that extended into the western Atlantic. After this merger, the tracking was stopped because the MCS was indistinguishable from the contiguous precipitation band. Fig. 1 shows the two-hour snapshots from the subjective tracking with the object boundary marked by a black contour. Though objective tracking is more desirable than a subjective method, most tracking algorithms define MCSs as contiguous precipitation areas. Such a traditional definition is not suitable for IMERG. Fig. 2 from the broader region shows multiple MCSs connected by low precipitation rates to form a single contiguous area that extends thousands of kilometers. This contiguous area cannot be defined as a single MCS.

236 The MCS from the June 6th case study undergoes multiple mergers and splits. We looked
237 at the IMERG animation repeatedly to discern the precipitation area that can be deemed an
238 MCS. If an embedded cell breaks away and merges with a neighboring MCS, we exclude it
239 from the MCS boundary in previous time steps. Similarly, if a cell joins with the MCS under
240 study, we include it within the object boundary in the previous time steps. The IMERG
241 animation is provided as supplemental material for the reader's reference. Choosing a
242 different MCS boundary by including or excluding small cells will somewhat affect metrics
243 such as area and rain volume; however, our conclusion remains the same.

244 On June 10th 2017, the DC-8 examined a small MCS in the western Atlantic near 73°W
245 and 25°N. Manual identification of the MCS boundary in IMERG was more straightforward
246 due to its isolated nature. This MCS was tracked until it dissipated on June 11th at 02:00 UTC
247 (Fig. 3).

248 For both MCSs, defined as IMERG objects, we compute the precipitation area,
249 volumetric rain rate, and maximum rain rate at each half-hour from IMERG precipitation.
250 The volumetric rain rate (mm km^2 hr^{-1}) at each grid cell is the product of the precipitation rate
251 and the area. For an MCS, it is the sum over all pixels in the MCS of the volumetric rain rate
252 at each pixel. Although rain volume is a time-integrated variable, we use it interchangeably
253 with the volumetric rain rate. Also, despite the technical difference between "precipitation"
254 and "rain", we use them interchangeably since all surface precipitation in these cases was
255 rain.

256 *b. Constructing precipitation rate distributions*

257 In section 4c, we examine the frequency distribution of precipitation rates for nearly the
258 full-length of the IMERG record and global tropics extending from 30°N to 30°S. Following
259 Tan et al. (2016, 2018) and Sungmin et al. (2017), we use a minimum threshold of 0.1 mm hr^{-}

260 ^{1} to determine if a grid cell is precipitating. We repeated this analysis for different thresholds
261 such as 0.2 and 0.3 mm hr^{-1} (figures not shown), and our conclusions are not sensitive to
262 these choices.

263 The precipitating grid cells are categorized into different sources based on variables
264 "HQprecipSource" and "IRkalmanFilterWeight", as discussed in section 2b. Then, a
265 precipitation rate distribution is computed for each source as a probability density function
266 (PDF) (Lamb and Verlinde, 2011). The resulting PDF will have the area under the curve
267 equal to 1.0.

268 In some analyses, IMERG sources are combined into two broad categories – "All PMW"
269 and "Morphing". The "All PMW" category includes instantaneous precipitation estimates
270 from all the PMW sensors and represents precipitation at locations with PMW observations.
271 The "Morphing" category represents precipitation estimates from the Kalman Filter at
272 locations without PMW observations, which could be either propagated PMW, IR, or
273 propagated PMW + IR. We also compute the precipitation rate distributions for these two
274 broad categories.

275 The long-term statistics are essential to remove temporal variations and detect the
276 systematic differences between PMW precipitation and morphing estimates. To reduce
277 computation, we randomly selected 19,000 half-hour IMERG data files from 2001 to 2019
278 (with 1000 files per year). The PDF computed for each half-hour file is averaged over 19,000
279 files to produce a mean distribution. To test if 19,000 files are an adequate sample size to
280 capture the systematic biases, we used a different random seed to select a new set of 19,000
281 half-hour files. The new sample set had PDFs similar to the original sample set with
282 negligible differences (figure not shown), implying that 19,000 half-hour data was sufficient.

283 *c. Computing precipitation occurrence (%)*

In the global tropics, only a percentage of grid cells receive precipitation in a 30-minute interval. The tropical precipitation occurrence varies temporally, and for the current climate, it will follow a certain distribution with a spread that represents the temporal variability. For each half-hour data, locations between 30°N and 30°S with and without PMW observations are grouped as "PMW" and "Morphing" grid cells, respectively. For each category, we determine precipitation occurrence, expressed as "percentage of grid cells with precipitation".

We compute precipitation occurrence for randomly selected 19,000 half-hour files from 2001 to 2019 (with1000 files per year). The histogram of precipitation occurrence for 19,000 half-hour data exhibits the variability in precipitation occurrence and the systematic bias between PMW precipitation and morphing estimates.

IMERG has precipitation rates below 10^{-3} mm hr^{-1}, so the precipitation occurrence depends on the choice of minimum threshold. We apply various subjective thresholds 0.1, 0.5, 1.0, and 2.0 mm hr^{-1} to understand their effects on precipitation occurrence.

4. Results

The following sub-sections describe differences in IMERG precipitation during and between PMW overpasses. First, we demonstrate the differences through two case studies investigated during the CPEX field campaign. Following the CPEX case studies, we use bulk statistics to confirm that the biases are systematic by comparing precipitation rate distributions between locations with and without PMW observations.

a. Case Study 1: June 6th 2017

The DC-8 aircraft mission on June 6th 2017, investigated a precipitation system extending from the central Gulf of Mexico northeastward to Florida's west coast. Fig. 4b and 4d show the aircraft's location, just before making its first penetration of the convective system, about

200 km off Florida's west coast. The aircraft track, position, and heading are overlaid on IR T_b and IMERG precipitation fields. We use the merged-IR product (Janowiak et al., 2001) available every 30 minutes centered on the hour and half-hour. For example, in Fig. 4b, the IR T_b at 19:00 UTC is from the observation period 18:45 to 19:15 UTC. However, the IMERG precipitation (Fig. 4d) is for the period 18:30 to19:00 UTC. We use the IR data at 19:00 UTC and not 18:30 UTC because it is closest to the aircraft observation at 18:48 UTC and PMW overpass at 18:53 UTC.

The forward camera has a minimum and maximum horizontal field of view (FOV) of 88° and 115°, respectively. They are marked on IMERG and IR images to reference the area being viewed. The forward camera (Fig. 4a) clearly shows vigorous mature convective towers extending well above the aircraft altitude of approximately 32,000 ft (9,800 m), which matches with heavily precipitating grid cells in IMERG. The pilot's radar also shows a long convective line oriented from southwest to northeast, similar to the precipitation band on IMERG. Table 1 provides the pilot radar's reflectivity scale and corresponding rainfall rates. IMERG precipitation for this period was retrieved from the Advanced Microwave Scanning Radiometer (AMSR-2), a PMW sensor, with an overpass around 18:53 UTC, which is close to the aircraft observation time at 18:48 UTC. These aircraft observations indicate that IMERG represents the observed convection qualitatively well at this PMW observation time. However, upon examination of the time-series of this MCS, we note discrepancies between the PMW overpasses.

The MCS is subjectively tracked in IMERG and its properties such as precipitation area, rain volume, and maximum rain rate are diagnosed as described in section 3a. Fig. 5 presents the time series of these MCS properties with PMW sensor names annotated on the x-axis if there is an overpass in that half-hour period. The time-series show that the MCS's maximum

precipitation rate peaks near 80 mm hr^{-1} several times when there are PMW overpasses. However, it 'sags' to about 40 mm hr^{-1} shortly before and after PMW overpasses. If we extend the MCS boundary to include adjacent cells, our conclusion doesn't change because most intense cells in the region are present within the current object boundary. The sagging of the maximum precipitation rate suggests a discrepancy between IMERG estimates from PMW observations and time morphing. If the MCS's maximum precipitation rate is linearly interpolated between two PMW observations, it would be a straight line connecting the peaks. However, it appears that the Kalman weighted averaging of propagated PMW and IR precipitation somehow creates this sag between the PMW overpasses, a concept that we will explore in section 5.

b. Case Study 2: June 10th 2017

On June 10th 2017, the DC-8 aircraft investigated a small MCS located over the western Atlantic, approximately 100 km in each direction (east-west and north-south). The system was probably in its most active growth phase when the DC-8 aircraft approached it at 19:14 UTC, at an altitude of 10 km. For the next three hours, the aircraft penetrated and circumnavigated the MCS as it rapidly matured and entered its decay phase. Fig. 6d shows the location of the DC-8 at 20:30 UTC, flying at an altitude of 10 km, and its track from the previous hour overlaid on IMERG precipitation. At 20:30 UTC, according to IMERG, the aircraft was about to penetrate a mesoscale region of light precipitation after the turn. However, a careful inspection of the forward camera's cloud photo shows no deep or stratiform clouds but only scattered shallow cumulus. The forward camera has a minimum and maximum diagonal FOV of 100° and 126°, respectively. This is more relevant than horizontal FOV since the aircraft was making a turn. These diagonal FOVs are marked on the IMERG and IR images (Fig 6b and 6d) as a reference to the area that the camera is observing.

In the cloud photo, the horizon is approximately 356 km away from the aircraft's location for the flight altitude of 10 km, limiting the area viewed by the forward camera. Though the camera's FOV is limited, it is evident from the cloud photo that the area ahead doesn't have widespread precipitation. The one-minute camera video (provided as supplemental material) covers a much larger area that clearly shows the scattered shallow cumulus over this region as the camera's FOV swept through it when the DC-8 made the turn. Also, the pilot's radar (Fig. 6c) shows no widespread reflectivity other than a small echo ahead of the aircraft, possibly from an isolated cumulus. Since reflectivity values below 20 dBZ would mean very light rain or none (Table 1), we cannot rely solely on the radar. On the IR image (Fig. 6b) from 20:30 UTC, which is closest to the aircraft observation time, we see no cold cloud top to the west of the MCS, where IMERG shows light precipitation. These pieces of evidence strongly suggest that the widespread light precipitation rates in IMERG on the west side of the MCS are spurious.

For this small MCS, Fig. 7 displays the time series of the precipitation area, rain volume, and maximum rain rate diagnosed from IMERG. In the half-hour period 20:00 to 20:30 UTC, the IMERG precipitation area jumped to three times its previous value. This sudden growth comes from a spurious precipitation area, identified as such from the aircraft photo, pilot's radar, and IR. To trace the origin of this false precipitation, we examined the source of IMERG precipitation estimates. Fig. 8 presents the MCS evolution from 19:30 through 23:00 UTC with the sources annotated in blue font. There were PMW observations at 19:30 and 23:00 UTC from a Microwave Humidity Sensor (MHS) and Special Sensor Microwave Imager/Sounder (SSMIS), respectively. At the time of the aircraft observation (18:30 UTC), the precipitation estimates were from the weighted average of propagated PMW and IR.

Hence this spurious precipitation is likely an artifact from the morphing algorithm, as will be discussed in section 5.

The precipitation area for the CPEX case study on June 6th (Fig. 5) also shows a sudden growth during half-hours, starting at 16:00 and 21:00 UTC, immediately after PMW overpasses. If we chose a different MCS boundary by including or excluding small neighboring cells, it affects the metrics. However, the area would still grow unrealistically, as clearly noticeable at 16:00 UTC in IMERG animation (provided as supplemental material). For both MCSs, if the precipitation areas were linearly interpolated between PMW overpasses, these sudden growths would not exist, and the MCS size would appear to grow more reasonably.

In both CPEX case studies, the unrealistic growth is not always present after a PMW observation. Similarly, the maximum precipitation rate for the June 10th case (Fig. 7) doesn't sag between PMW observations from 18:00 to 20:00 UTC. This contrasts with the CPEX case on June 6th 2017, where the maximum precipitation rate peaked during most PMW observations and sagged between overpass times (Fig. 5). Thus, these examples also suggest that the morphing issues uncovered are not uniformly present.

c. Precipitation rate distribution: PMW vs. Morphing

Given the apparent limitations in IMERG Version 06 revealed by this analysis of two MCSs from the CPEX field program, we explore the systematic biases in IMERG precipitation using bulk statistics. Specifically, we look at the precipitation rate distribution (as a probability density function) of PMW observations and morphing over a wider region from 30°N to 30°S and for an extended period of 19 years. Our initial analysis showed that

401 TMI and GMI exhibit differences in their precipitation rate distribution, so the data are
402 grouped into TRMM (2001 – 2013) and GPM (2015-2019) periods. In the year 2014, PMW
403 sensors are inter-calibrated to TMI for dates before June 1st and to GMI for the rest of the
404 year, so 2014 is excluded to avoid mixing the calibrations. The PDF differences between TMI
405 and GMI are not analyzed further, since this is beyond the scope of this study.

406 The precipitation rate distributions from both the TRMM and GPM periods (Fig. 9) show
407 that differences between PMW sensors are very small as expected, since they are inter-
408 calibrated to TMI or GMI histograms. However, differences between distributions for PMW
409 and morphed precipitation stand out compared to differences between individual sensors. We
410 can infer from Fig. 9 that the morphing estimates have a higher frequency of light
411 precipitation rates and a lower frequency of heavy precipitation rates relative to PMW
412 estimates. This conclusion is similar to the result from the CPEX mission on June 10th 2017,
413 where the small MCS observed at 20:30 UTC had spurious precipitation areas with light
414 precipitation rates.

415 Another important conclusion from the CPEX case study on June 6th 2017 (Fig. 5) was
416 that the MCS's maximum precipitation rate decreased further and further as the time interval
417 from the PMW overpass increased. Fig. 10 presents precipitation rate distributions for time
418 intervals away from the PMW overpass (both past and future). The time interval "30 mins
419 away" represents time morphing estimates from the past PMW observations propagated
420 forward to the next half-hour and future PMW observations propagated backward to the
421 previous half-hour. Similar logic can be extended to other time intervals. The distributions
422 show that the frequency of light precipitation increases slightly with increasing time intervals.
423 In contrast, there is a prominent decrease in the frequency of heavy precipitation rates, as one
424 moves further away from the PMW overpass times. This conclusion is consistent with the

425 observed sag in the maximum precipitation rate away from PMW overpasses in the CPEX
426 case study on June 6th 2017.

427

428 *d. Precipitation Occurrence: PMW vs. Morphing*

429 Fig. 11. displays histograms of PMW and morphing precipitation occurrence from 19,000
430 half-hour data for different minimum thresholds (0.1, 0.5, 1.0, and 2.0 mm hr^{-1}). The spatial
431 coverage of PMW sensors changes with time as they move over various regions on the earth.
432 This introduces spatial variability and sampling variability in the tropical precipitation
433 occurrence. Therefore, the spread in the histogram represents all three variabilities: temporal,
434 spatial, and PMW coverage. The statistic "precipitation occurrence" also can be interpreted as
435 the sum of frequencies of various precipitation rate bins in Fig. 9 expressed as a fraction of
436 total grid cells in each category. This statistic is more intuitive and highlights the net effect of
437 morphing on tropical precipitation occurrence.

438 For a minimum threshold of 0.1 mm hr^{-1}, Fig. 11a shows that locations with PMW
439 observations have a 6.56% median precipitation occurrence, whereas locations with estimates
440 from morphing have an 8.86% median precipitation occurrence. This difference is
441 considerable and implies that morphing creates 35% more precipitation for a same-sized
442 region. Using a non-parametric significance test (permutation test; Wilks 2011), we found
443 that the difference in median precipitation occurrence between PMW and morphing is
444 statistically significant at a 99% confidence interval. This suggests that the difference in
445 precipitation occurrence between PMW and morphing is substantially larger than the
446 variabilities or spread in the histogram. The higher precipitation occurrence in morphing
447 estimates implies that it produces spurious precipitation cells, consistent with the CPEX case
448 study from June 10th 2017.

449 When the minimum threshold is increased to 0.5 mm hr^{-1}, the absolute and relative
450 difference in precipitation occurrence between PMW and morphing decreases sharply (Fig.
451 11b). Results across the range of minimum thresholds (0.1, 0.5, 1.0, and 2.0 mm hr^{-1}) show
452 that light rain rates contribute to the significant difference in precipitation occurrence
453 between PMW and morphing.

454 ## 5. Discussion

455 The specific instances of spurious precipitation in the CPEX case can be traced back to
456 the time morphing algorithm. In general, a precipitation system observed at two different
457 times will often have different sizes and shapes of precipitation areas. At intermediate times,
458 the morphing algorithm propagates these PMW observations in the forward and backward
459 direction using motion vectors with "little change" in their shape and size. Even if the motion
460 vectors place the centroid of a forward and backward propagated system on top of each other,
461 the weighted averaging will create a larger area if the shapes are different. In addition, the
462 increase in precipitation area may be exacerbated if the motion vectors have biases that offset
463 the centroids of the forward and backward propagated systems.

464 The overlapping of different sizes and shapes from two observation times can explain the
465 unrealistic growth sometimes observed in CPEX case studies. The precipitation area created
466 from overlapping shapes is larger at intermediate times and suddenly changes to a smaller
467 area at the closest PMW observation This might show up as a sudden decay or growth in
468 precipitation area immediately before or after PMW observations, as observed in the CPEX
469 case studies.

470 Though overlaps produce larger areas at intermediate times, the propagated precipitation
471 rates are reduced by their Kalman weights that are roughly inversely proportional to

472 propagation time (Joyce et al. 2011). Some grid cells in the intersecting region of forward and
473 backward propagated precipitation areas receive estimates from both. However, other cells
474 receive estimates from only one. Though the morphing algorithm combines propagated
475 precipitation with IR precipitation, the Kalman averaging will more likely produce light rain
476 in grid cells with the contribution from only one input source. For example, say that the
477 weights for forward propagated, backward propagated, and IR in a particular grid cell are
478 0.26,0.34, and 0.40, respectively. If the grid cell's only non-zero contribution is forward
479 propagated precipitation of 2 mm hr^{-1}, the Kalman averaging would estimate a value of 0.52
480 mm hr^{-1} (0.26 * 2 + 0.34 * 0 + 0.40 * 0).

481 Fig. 8 shows the MCS from the CPEX case study on June 10th 2017, exhibiting different
482 shapes and sizes during PMW observations at 19:30 and 23:00 UTC from a Microwave
483 Humidity Sensor (MHS) and Special Sensor Microwave Imager/Sounder (SSMIS),
484 respectively. At the intermediate times, the MCS takes a shape and size that is an overlap of
485 these "PMW observations" propagated to the respective analysis time. At 20:30 UTC, the
486 west side of the MCS must be provided by the backward propagated precipitation because the
487 IR image (Fig. 6b) shows no deep convection, and the forward propagated PMW observation
488 from 19:30 UTC has no rainfall over this region. The intensity of backward propagation of
489 PMW precipitation fell from 2 mm hr^{-1} to 0.5 mm hr^{-1} on the west side of the MCS due to
490 decreasing Kalman weights and lack of other sources. The aircraft photos and IR image in
491 Fig. 6 show that the IMERG precipitation on the west side of the MCS is indeed spurious at
492 20:30 UTC.

493 IMERG, with its high temporal resolution, is more suitable than the past gridded
494 precipitation data to track MCSs as precipitation objects and study their upscale growth.
495 Understanding the IMERG biases presented in this article might help define MCSs and their

upscale growth, more appropriately. This study shows that using rain volume to define the growth and decay of an MCS yields stable results, based on the CPEX case studies. In contrast, the use of precipitation area to define the MCS life cycle is sometimes contaminated by spurious precipitation. This can be remedied to some extent by using a low-end cutoff precipitation threshold. Figs. 9 and 11 suggest that a precipitation map thresholded at or above 0.5 mm hr^{-1} has minimal spurious rain areas. However, one should use the cutoff cautiously because it merely sets the low end of the PDF to zero, but it cannot recover the underestimation at the high end. Taken together, a cutoff will cause the overall mean and rain volume of the morphed estimates to be underestimated. The problem is more fundamental and affects the entire PDF.

This line of reasoning was developed in conversations with the IMERG team, leading them to develop a new algorithm called Scheme for Histogram Adjustment with Ranked Precipitation Estimates Neighborhood (SHARPEN) that resolves some of the biases reported here. This algorithm restores the precipitation rate distribution of morphing estimates to a distribution similar to the PMW estimates using a quantile mapping based approach. SHARPEN will most likely be implemented in the upcoming release of IMERG Version 07, and is described in the companion paper (Tan et al. 2021). Preliminary testing (not shown) demonstrated that SHARPEN reduced the spurious precipitation considerably for the June 10^{th} CPEX case study.

6. Conclusions

In this study, an object-oriented approach is used to compare MCS properties, such as precipitation area, rain volume, and maximum precipitation rate during and between PMW

519 observations. Two case studies are used to investigate and illustrate potential issues with the
520 time morphing in IMERG before these issues are confirmed to be prevalent throughout
521 IMERG using bulk statistics

522 In the case studies, IMERG precipitation is evaluated against DC-8 aircraft observations
523 from the NASA CPEX field program. The aircraft photos, pilot radar, and IR image indicate
524 that at times of PMW observations, IMERG precipitation area is similar to aircraft
525 observations. However, in the absence of PMW observations, IMERG appeared to have
526 spurious precipitation areas. For the small MCS of June 10th 2017, the precipitation area grew
527 unrealistically in the next 30 minutes after the PMW observation at 19:30 UTC. We found
528 that this sudden growth and the spurious precipitation originates from the morphing
529 algorithm. Another finding was that for the intense, large MCS of June 6th 2017, the
530 maximum precipitation rate peaked at most PMW overpass times, but sagged between those
531 observation times. Although these are limited case studies, the evidence from CPEX guided
532 us to investigate systematic biases in the IMERG's time morphing algorithm. The analysis of
533 precipitation rate distribution and precipitation occurrence shows that there are systematic
534 differences between precipitation estimates from PMW observations and time morphing.
535 When PMW observations are absent, IMERG has a higher frequency of light precipitation
536 and a lower occurrence of heavy precipitation rates. The high occurrence of light
537 precipitation rates may sometimes produce large precipitation areas.

538 In our work, we highlight biases in time morphed precipitation estimates compared to
539 PMW precipitation. However, PMW precipitation estimates from GPROF have their own
540 biases as highlighted in past studies. An ideal validation would be to compare morphing
541 precipitation estimates with surface observations. Nevertheless, in the absence of global
542 surface observations, comparing IMERG precipitation estimates for PMW observation and

time morphing is still valuable to bring out their algorithmic differences. Identifying these morphing biases helped the IMERG team improve the next version of IMERG by bringing the morphing estimates more into line with the PMW (and PMW-calibrated IR) estimates. The end users of IMERG Version 06 should be cautious about the higher occurrence of light precipitation and lower precipitation intensity in the absence of PMW observations.

Acknowledgments.

We appreciate the skill and dedication of the pilots, flight crews, instrument teams, and NASA supporting staff that made the CPEX field program successful. We are grateful for discussions on statistical techniques with Prof. Courtney Strong and Prof. Gannet Hallar at the Department of Atmospheric Sciences, University of Utah. We also thank the three anonymous reviewers whose comments and suggestions helped refine this manuscript. We appreciate the computing and storage support from the Center for High-Performance Computing (CHPC) at the University of Utah. This research was supported by NASA Grant NNX17AG74G (Univ. of Utah) and the GPM mission (G. Huffman) under the leadership of Ramesh Kakar and Gail Jackson.

Data Availability Statement.

The aircraft track from the NASA's CPEX field program flights is accessible at https://tcis.jpl.nasa.gov/data/cpex/track/. The aircraft's forward camera and pilots' radar videos from the CPEX program are available at https://asp-archive.arc.nasa.gov/CPEX/Video/. IMERG is a NASA's global satellite precipitation product available at different time resolution and latencies. IMERG Version 06 (Final Run) used in this study can be downloaded from the

https://disc.gsfc.nasa.gov/datasets/GPM_3IMERGHH_06/summary?keywords=%22IMERG%20final%22. The web interface allows a user to choose the appropriate period (2001-2019) and the domain (30°N – 30°S).

REFERENCES

Adler, R.F.; Sapiano, M.R.P.; Huffman, G.J.; Wang, J.-J.; Gu, G.; Bolvin, D.; Chiu, L.; Schneider, U.; Becker, A.; Nelkin, E.; Xie, P.; Ferraro, R.; Shin, D.-B. The Global Precipitation Climatology Project (GPCP) Monthly Analysis (New Version 2.3) and a Review of 2017 Global Precipitation. *Atmosphere* 2018, *9*, 138.

Akaeda, K., J. Reisner, and D. Parsons, 1995: The Role of Mesoscale and Topographically Induced Circulations in Initiating a Flash Flood Observed during the TAMEX Project. *Mon. Wea. Rev.*, **123**, 1720–1739, https://doi.org/10.1175/1520-0493(1995)123<1720:TROMAT>2.0.CO;2.

Asong, Z. E., S. Razavi, H. S. Wheater, and J. S. Wong, 2017: Evaluation of Integrated Multisatellite Retrievals for GPM (IMERG) over Southern Canada against Ground Precipitation Observations: A Preliminary Assessment. *J. Hydrometeor.*, **18**, 1033–1050, https://doi.org/10.1175/JHM-D-16-0187.1.

Bodenreider, C., Wright, L., Barr, O., Xu, K., & Wilson, S. (2019). Assessment of social, economic, and geographic vulnerability pre-and post-hurricane Harvey in Houston, *Texas. Environmental Justice*, 12(4), 182-193. http://doi.org/10.1089/env.2019.0001.

Bytheway, J. L., M. Hughes, K. Mahoney, and R. Cifelli, 2020: On the Uncertainty of High-Resolution Hourly Quantitative Precipitation Estimates in California. *J. Hydrometeor.*, **21**, 865–879, https://doi.org/10.1175/JHM-D-19-0160.1.

589 Cui, W., X. Dong, B. Xi, Z. Feng, and J. Fan, 2020: Can the GPM IMERG Final Product
590 Accurately Represent MCSs' Precipitation Characteristics over the Central and Eastern
591 United States?. *J. Hydrometeor.*, **21**, 39–57, https://doi.org/10.1175/JHM-D-19-0123.1.

592 Davis, C., B. Brown, and R. Bullock, 2006: Object-Based Verification of Precipitation
593 Forecasts. Part I: Methodology and Application to Mesoscale Rain Areas. *Mon. Wea.*
594 *Rev.*, **134**, 1772–1784, https://doi.org/10.1175/MWR3145.1.

595 Gaona, M. F. R., A. Overeem, H. Leijnse, and R. Uijlenhoet, 2016: First-Year Evaluation of
596 GPM Rainfall over the Netherlands: IMERG Day 1 Final Run (V03D). *J. Hydrometeor.*,
597 **17**, 2799–2814, https://doi.org/10.1175/JHM-D-16-0087.1.

598 Gelaro, R., and Coauthors, 2017: The Modern-Era Retrospective Analysis for Research and
599 Applications, Version 2 (MERRA-2). *J. Climate*, **30**, 5419–5454,
600 https://doi.org/10.1175/JCLI-D-16-0758.1.

601 Gowan, T. A., and J. D. Horel, 2020: Evaluation of IMERG-E Precipitation Estimates for
602 Fire Weather Applications in Alaska. *Wea. Forecasting*, **35**, 1831–1843,
603 https://doi.org/10.1175/WAF-D-20-0023.1.

604 Gu, G., R. F. Adler, G. J. Huffman, and S. Curtis, 2007: Tropical Rainfall Variability on
605 Interannual-to-Interdecadal and Longer Time Scales Derived from the GPCP Monthly
606 Product. *J. Climate*, **20**, 4033–4046, https://doi.org/10.1175/JCLI4227.1.

607 Hayden, L., and C. Liu, 2018: A Multiyear Analysis of Global Precipitation Combining
608 CloudSat and GPM Precipitation Retrievals. *Journal of Hydrometeor.*, **19**,12, 1935-1952,
609 https://doi.org/10.1175/JHM-D-18-0053.1

610 Hong, Y., K. Hsu, S. Sorooshian, and X. Gao, 2004: Precipitation Estimation from Remotely
611 Sensed Imagery Using an Artificial Neural Network Cloud Classification System. *J. Appl.*
612 *Meteor.*, **43**, 1834–1853, https://doi.org/10.1175/JAM2173.1.

613 Hou, A. Y., and Coauthors, 2014: The Global Precipitation Measurement Mission. *Bull.*
614 *Amer. Meteor. Soc.*, **95**, 701–722, https://doi.org/10.1175/BAMS-D-13-00164.1.

615 Huffman, G. J., and Coauthors, 1997: The Global Precipitation Climatology Project (GPCP)
616 Combined Precipitation Dataset. *Bull. Amer. Meteor. Soc.*, **78**, 5–20,
617 https://doi.org/10.1175/1520-0477(1997)078<0005:TGPCPG>2.0.CO;2.

618 ——, and Coauthors, 2007: The TRMM Multisatellite Precipitation Analysis (TMPA):
619 Quasi-Global, Multiyear, Combined-Sensor Precipitation Estimates at Fine Scales. *J.*
620 *Hydrometeor.*, **8**, 38–55, https://doi.org/10.1175/JHM560.1.

621 ——, and Coauthors, 2019a: NASA Global Precipitation Measurement (GPM) Integrated
622 Multi-satellitE Retrievals for GPM (IMERG). Algorithm Theoretical Basis Doc., version
623 4.6, 28 pp., https://gpm.nasa.gov/resources/documents/algorithm-information/IMERG-
624 V06-ATBD.

625 ——, and Coauthors, 2019b: Integrated Multi-Satellite Retrievals for GPM (IMERG)
626 technical documentation. NASA Tech. Doc., 77 pp.,
627 https://gpm.nasa.gov/resources/documents/IMERG-V06-Technical-Documentation.

628 Janowiak, J. E., Joyce, R. J., and Yarosh, Y. (2001). A Real-Time Global Half-Hourly Pixel-
629 Resolution Infrared Dataset and Its Applications. *Bulletin of the American Meteorological*
630 *Society* 82, 2, 205-218, https://doi.org/10.1175/1520-
631 0477(2001)082<0205:ARTGHH>2.3.CO;2

632 Johnson, A., X. Wang, F. Kong, and M. Xue, 2013: Object-Based Evaluation of the Impact of
633 Horizontal Grid Spacing on Convection-Allowing Forecasts. *Mon. Wea. Rev.*, **141**, 3413–
634 3425, https://doi.org/10.1175/MWR-D-13-00027.1.

635 Joyce, R. J., J. E. Janowiak, P. A. Arkin, and P. Xie, 2004: CMORPH: A Method that
636 Produces Global Precipitation Estimates from Passive Microwave and Infrared Data at
637 High Spatial and Temporal Resolution. *J. Hydrometeor.*, **5**, 487–503,
638 https://doi.org/10.1175/1525-7541(2004)005<0487:CAMTPG>2.0.CO;2.

639 ——, and P. Xie, 2011: Kalman Filter–Based CMORPH. *J. Hydrometeor.*, **12**, 1547–1563,
640 https://doi.org/10.1175/JHM-D-11-022.1.

641 Kidd, C, Tan, J, Kirstetter, P-E, Petersen, WA. Validation of the Version 05 Level 2
642 precipitation products from the GPM Core Observatory and constellation satellite sensors.
643 *Q J R Meteorol Soc* 2018a; 144 (Suppl. 1): 313– 328. https://doi.org/10.1002/qj.3175.

644 ——**,** 2018b: Algorithm Theoretical Basis Document (ATBD) Version 01-02 for the NASA
645 Global Precipitation Measurement (GPM) Precipitation Retrieval and Profiling Scheme
646 (PRPS). GPM Project, Greenbelt, MD, 16.

647 Kummerow, C., W. Barnes, T. Kozu, J. Shiue, and J. Simpson, 1998: The Tropical Rainfall
648 Measuring Mission (TRMM) Sensor Package. *J. Atmos. Oceanic Technol.*, **15**, 809–817,
649 https://doi.org/10.1175/1520-0426(1998)015<0809:TTRMMT>2.0.CO;2.

650 ——. D., D. L. Randel, M. Kulie, N. Wang, R. Ferraro, S. Joseph Munchak, and V. Petkovic,
651 2015: The Evolution of the Goddard Profiling Algorithm to a Fully Parametric Scheme. *J.*
652 *Atmos. Oceanic Technol.*, 32, 2265–2280, https://doi.org/10.1175/JTECH-D-15-0039.1.

653 Lamb, D., and J.Verlinde, 2011: *The Physics and Chemistry of Clouds*. Cambridge University
654 Press, 70 pp.

655 Liu, C., 2011: Rainfall Contributions from Precipitation Systems with Different Sizes,
656 Convective Intensities, and Durations over the Tropics and Subtropics. *J. Hydrometeor.*,
657 **12**, 394–412, https://doi.org/10.1175/2010JHM1320.1.

658 Maranan, M., A. H. Fink, P. Knippertz, L. K. Amekudzi, W. A. Atiah, and M. Stengel, 2020:
659 A Process-Based Validation of GPM IMERG and Its Sources Using a Mesoscale Rain
660 Gauge Network in the West African Forest Zone. *J. Hydrometeor.*, **21**, 729–749,
661 https://doi.org/10.1175/JHM-D-19-0257.1.

662 McCollum, D. M., R. A. Maddox, and K. W. Howard, 1995: Case Study of a Severe
663 Mesoscale Convective System in Central Arizona. *Wea. Forecasting*, **10**, 643–665,
664 https://doi.org/10.1175/1520-0434(1995)010<0643:CSOASM>2.0.CO;2.

665 Mohr, K. I., J. S. Famiglietti, and E. J. Zipser, 1999: The Contribution to Tropical Rainfall
666 with respect to Convective System Type, Size, and Intensity Estimated from the 85-GHz
667 Ice-Scattering Signature. *J. Appl. Meteor.*, **38**, 596–606, https://doi.org/10.1175.

668 Nesbitt, S. W., R. Cifelli, and S. A. Rutledge, 2006: Storm Morphology and Rainfall
669 Characteristics of TRMM Precipitation Features. *Mon. Wea. Rev.*, **134**, 2702–2721,
670 https://doi.org/10.1175/MWR3200.1.

671 Nguyen, P., M. Ombadi, S. Sorooshian, K. Hsu, A. AghaKouchak, D. Braithwaite, H.
672 Ashouri, and A. R. Thorstensen, 2018: The PERSIANN family of global satellite
673 precipitation data: A review and evaluation of products. *Hydrol. Earth Syst. Sci.*, 22,
674 5801–5816, https://doi.org/10.5194/hess-22-5801-2018.

675 Olson, W. S., Masunaga, H., & the GPM Combined Radar-Radiometer Algorithm Team.
676 (2011). GPM combined radar-radiometer precipitation. Algorithm theoretical basis
677 document (Version 2). PPS, NASA/GSFC, 58 pp. Available at

http://pps.gsfc.nasa.gov/Documents/GPM2011CombinedL2ATBD.pdf, last accessed 17 Nov 2018.

Paul, S., Ghebreyesus, D., & Sharif, H. O. (2019). Brief communication: Analysis of the fatalities and socio-economic impacts caused by Hurricane Florence. Geosciences, 9(2), 58. https://doi.org/10.3390/geosciences9020058.

Randel D.L., Kummerow C.D., Ringerud S. (2020) The Goddard Profiling (GPROF) Precipitation Retrieval Algorithm. In: Levizzani V., Kidd C., Kirschbaum D., Kummerow C., Nakamura K., Turk F. (eds) *Satellite Precipitation Measurement*. Advances in Global Change Research, vol 67. Springer, Cham.

Schneider, U., Becker, A., Finger, P. *et al.* GPCC's new land surface precipitation climatology based on quality-controlled in situ data and its role in quantifying the global water cycle. *Theor Appl Climatol* **115,** 15–40 (2014). https://doi.org/10.1007/s00704-013-0860-x.

Sharifi, E., R. Steinacker, and B. Saghafian, 2016: Assessment of GPM-IMERG and other precipitation products against gauge data under different topographic and climatic conditions in Iran: Preliminary results. *Remote Sens.*, 8, 135, https://doi.org/10.3390/rs8020135.

Sohoulande, C. D., Stone, K., Szogi, A., & Bauer, P. (2019). An investigation of seasonal precipitation patterns for rainfed agriculture in the Southeastern region of the United States. *Agricultural Water Management*, 223, 105728. https://doi.org/10.1016/j.agwat.2019.105728.

699 Steinker, S., Hoberg, K., & Thonemann, U. W. (2017). The value of weather information for
700 e-commerce operations. *Production and Operations Management*, 26(10), 1854-1874.
701 https://doi.org/10.1111/poms.12721.

702 Sungmin, O., Foelsche, U., Kirchengast, G., Fuchsberger, J., Tan, J., & Petersen, W. A.
703 (2017). Evaluation of GPM IMERG Early, Late, and Final rainfall estimates using
704 WegenerNet gauge data in southeastern Austria. *Hydrology & Earth System Sciences*,
705 *21*(12).

706 Tan, J., W. A. Petersen, and A. Tokay, 2016: A Novel Approach to Identify Sources of Errors
707 in IMERG for GPM Ground Validation. *J. Hydrometeor.*, **17**, 2477–2491,
708 https://doi.org/10.1175/JHM-D-16-0079.1.

709 ——, W. A. Petersen, P. Kirstetter, and Y. Tian, 2017: Performance of IMERG as a Function
710 of Spatiotemporal Scale. *J. Hydrometeor.*, **18**, 307–319, https://doi.org/10.1175/JHM-D-
711 16-0174.1.

712 ——, W. A. Petersen, G. Kirchengast, D. C. Goodrich, and D. B. Wolff, 2018: Evaluation of
713 Global Precipitation Measurement Rainfall Estimates against Three Dense Gauge
714 Networks. *J. Hydrometeor.*, **19**, 517–532, https://doi.org/10.1175/JHM-D-17-0174.1.

715 ——, G. J. Huffman, D. T. Bolvin, and E. J. Nelkin, 2019: IMERG V06: Changes to the
716 Morphing Algorithm. *J. Hydrometeor.*, submitted

717 ——, G. J. Huffman, D. T. Bolvin, and E. J. Nelkin, M. Rajagopal, 2021: SHARPEN: A
718 Scheme to Restore the Distribution of Averaged Precipitation Fields. *J. Hydrometeorol.*,
719 submitted.

720 Tapiador, F. J., A. Navarro, E. García-Ortega, A. Merino, J. L. Sánchez, C. Marcos, and C.
721 Kummerow, 2020: The Contribution of Rain Gauges in the Calibration of the IMERG
722 Product: Results from the First Validation over Spain. *J. Hydrometeor.*, **21**, 161–182,
723 https://doi.org/10.1175/JHM-D-19-0116.1.

724 Verstraete, G., Aghezzaf, E. H., & Desmet, B. (2019). A data-driven framework for
725 predicting weather impact on high-volume low-margin retail products. Journal of
726 Retailing and Consumer Services, 48, 169-177.
727 https://doi.org/10.1016/j.jretconser.2019.02.019.

728 Watters, D., A. Battaglia, K. Mroz, and F. Tridon, 2018: Validation of the GPM Version-5
729 Surface Rainfall Products over Great Britain and Ireland. *J. Hydrometeor.*, **19**, 1617–
730 1636, https://doi.org/10.1175/JHM-D-18-0051.1.

731 Wilks, D. S., 2011: *Statistical Methods in the Atmospheric Sciences*. 3rd ed. Elsevier, 169 pp.

732 Xie, P., R. Joyce, S. Wu, S. Yoo, Y. Yarosh, F. Sun, and R. Lin, 2017: Reprocessed, Bias-
733 Corrected CMORPH Global High-Resolution Precipitation Estimates from 1998. *J.*
734 *Hydrometeor.*, **18**, 1617–1641, https://doi.org/10.1175/JHM-D-16-0168.1.

735 You, Y., V. Petkovic, J. Tan, R. Kroodsma, W. Berg, C. Kidd, and C. Peters-Lidard, 2020:
736 Evaluation of V05 Precipitation Estimates from GPM Constellation Radiometers Using
737 KuPR as the Reference. *J. Hydrometeor.*, **21**, 705–728, https://doi.org/10.1175/JHM-D-
738 19-0144.1.

739 Zhang, Q., Sun, P., Singh, V. P., & Chen, X. (2012). Spatial-temporal precipitation changes
740 (1956–2000) and their implications for agriculture in China. *Global and Planetary*
741 *Change*, 82, 86-95. https://doi.org/10.1016/j.gloplacha.2011.12.001.

742 Zhou, Y., W. K. M. Lau, and G. J. Huffman, 2015: Mapping TRMM TMPA into Average
743 Recurrence Interval for Monitoring Extreme Precipitation Events. *J. Appl. Meteor.*
744 *Climatol.*, **54**, 979–995, https://doi.org/10.1175/JAMC-D-14-0269.1.

745

746

File generated with AMS Word template 1.0

747 TABLES

748

Color	**Returns**	**Reflectivity (dBZ)**	**Rainfall Rate (mm hr^{-1})**
Black	Very light, or None	< 20	< 0.7
Green	Light	20 – 30	0.7– 4
Yellow	Medium	30 – 40	4 – 12
Red	Strong	>= 40	> 12
Magenta	Turbulence	N/A	N/A

749 Table 1. DC-8 aircraft pilot's radar reflectivity codes (for signal gain set at calibration)

750 based on IntuVue RDR-4000 Weather Radar Pilot's Guide.

751

File generated with AMS Word template 1.0

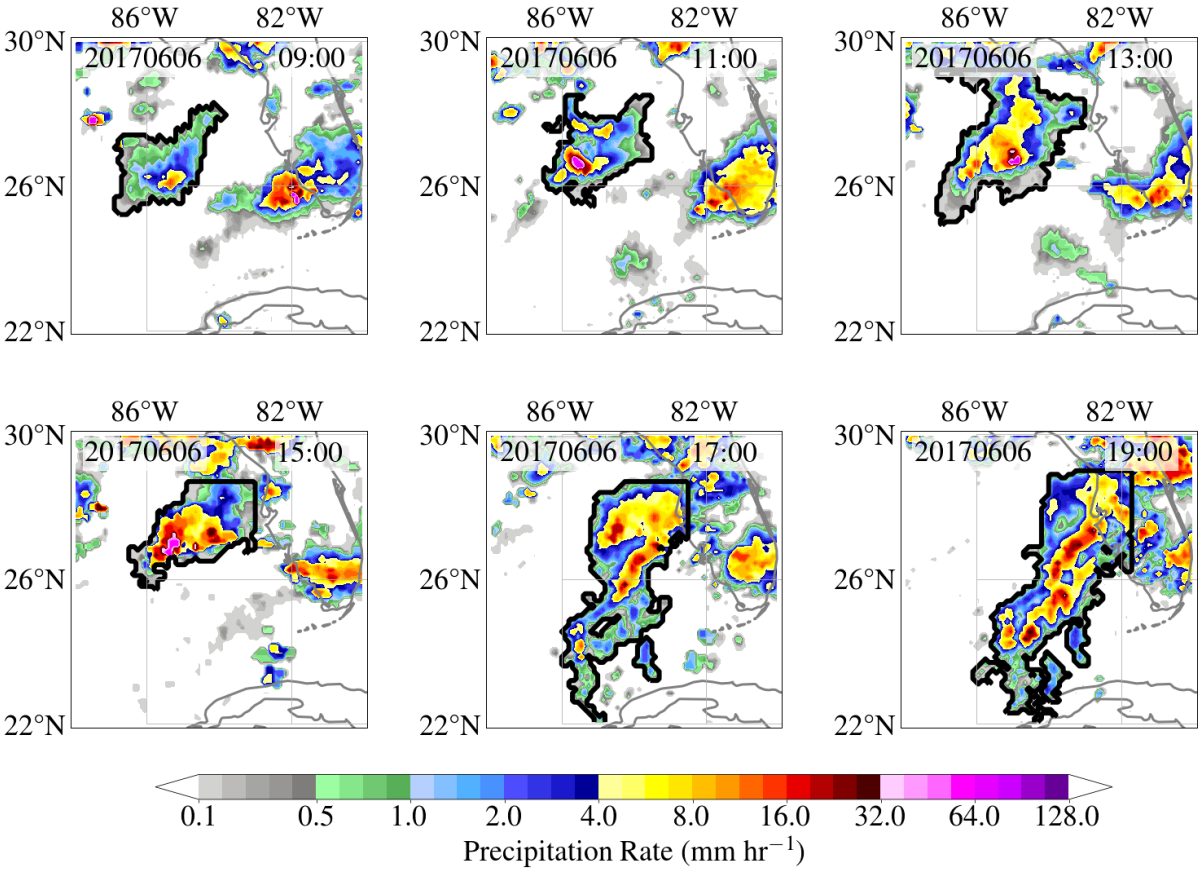

752

753 Fig. 1. The MCS observed on June 6th 2017, during the CPEX field program, is tracked as the IMERG precipitation
754 object from 09:00 to 22:00 UTC. The multi-panel figure shows a snapshot every two hours with the object
755 boundary denoted by a black contour.

756

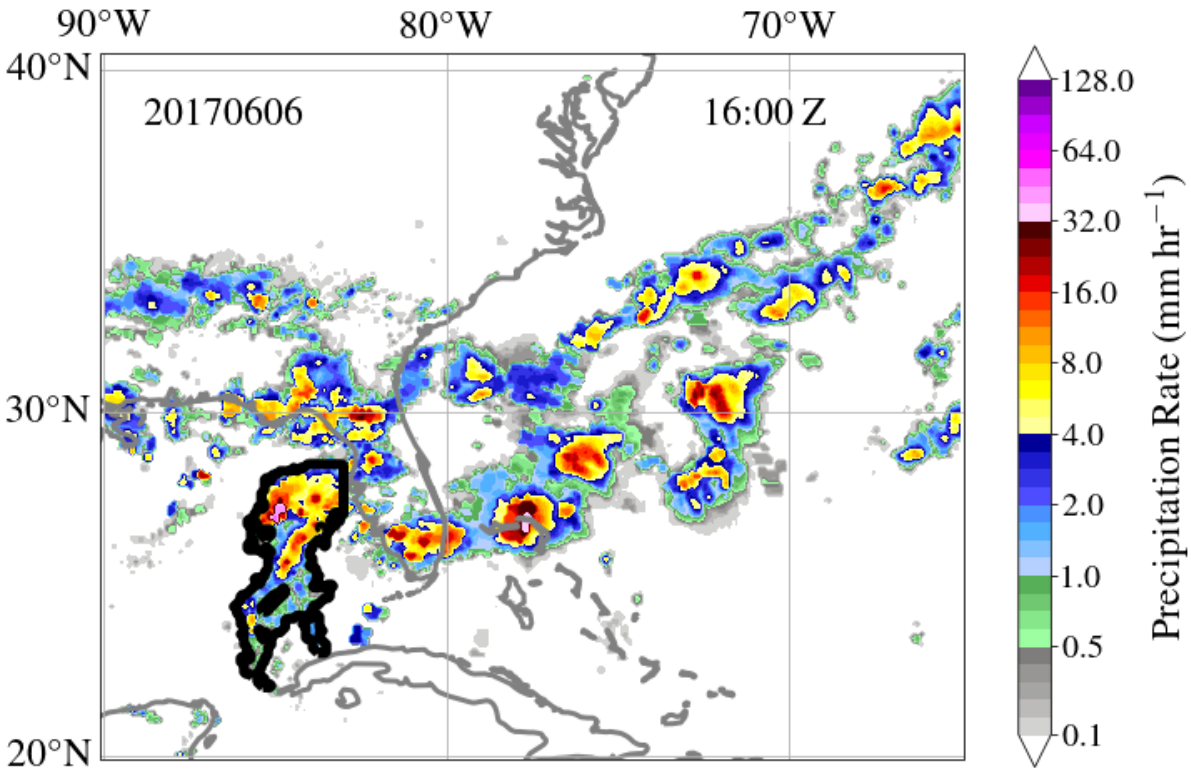

757

758 Fig. 2. The MCS from the CPEX case study on June 6th 2017, marked by a black contour, is connected to the
759 neighboring MCSs by low precipitation rates. If the traditional object definition of contiguous area is used, the
760 MCS will span thousands of kilometers.

761

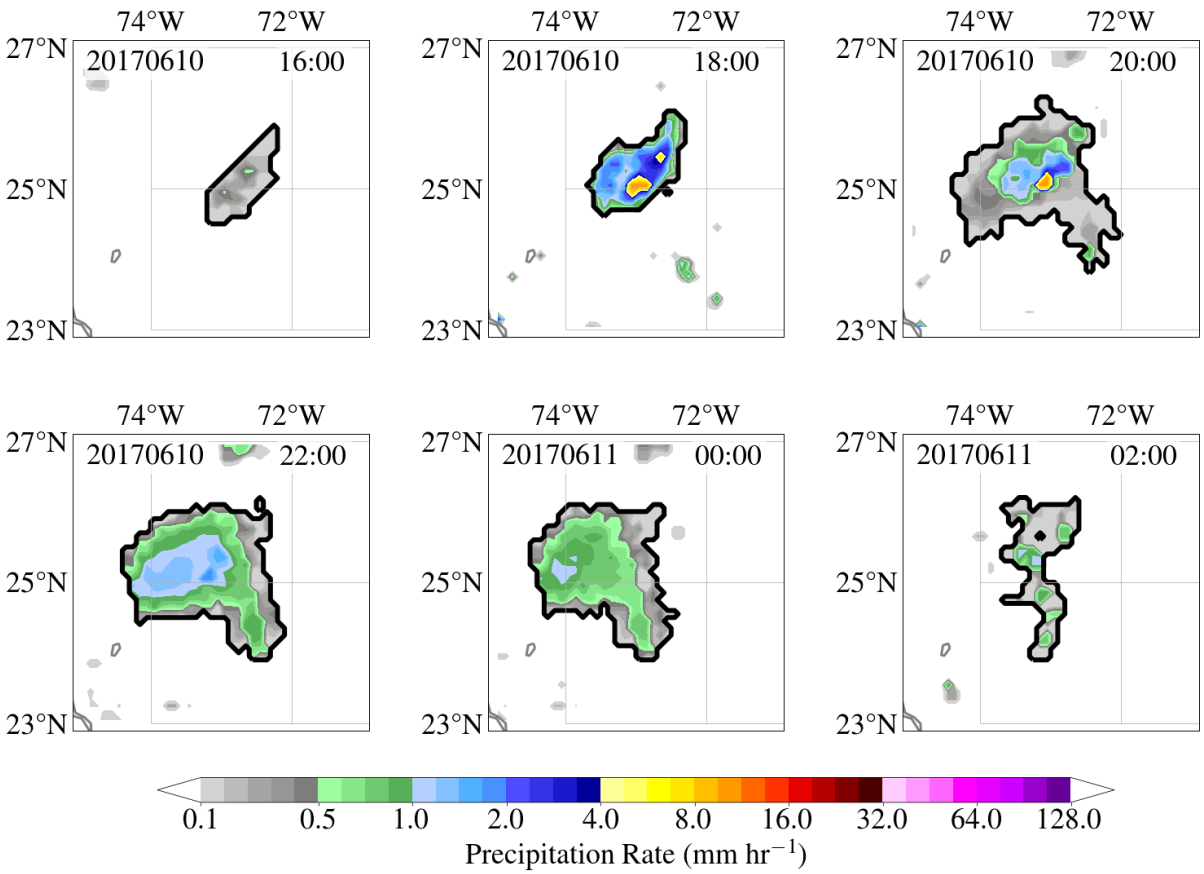

762

763 Fig. 3. The MCS observed on June 10th 2017, during the CPEX field program, is tracked as the IMERG
764 precipitation object from 16:00 to 02:00 UTC the next day. The multi-panel figure shows two-hour snapshots with
765 MCS boundary marked by a black contour.

766
767
768

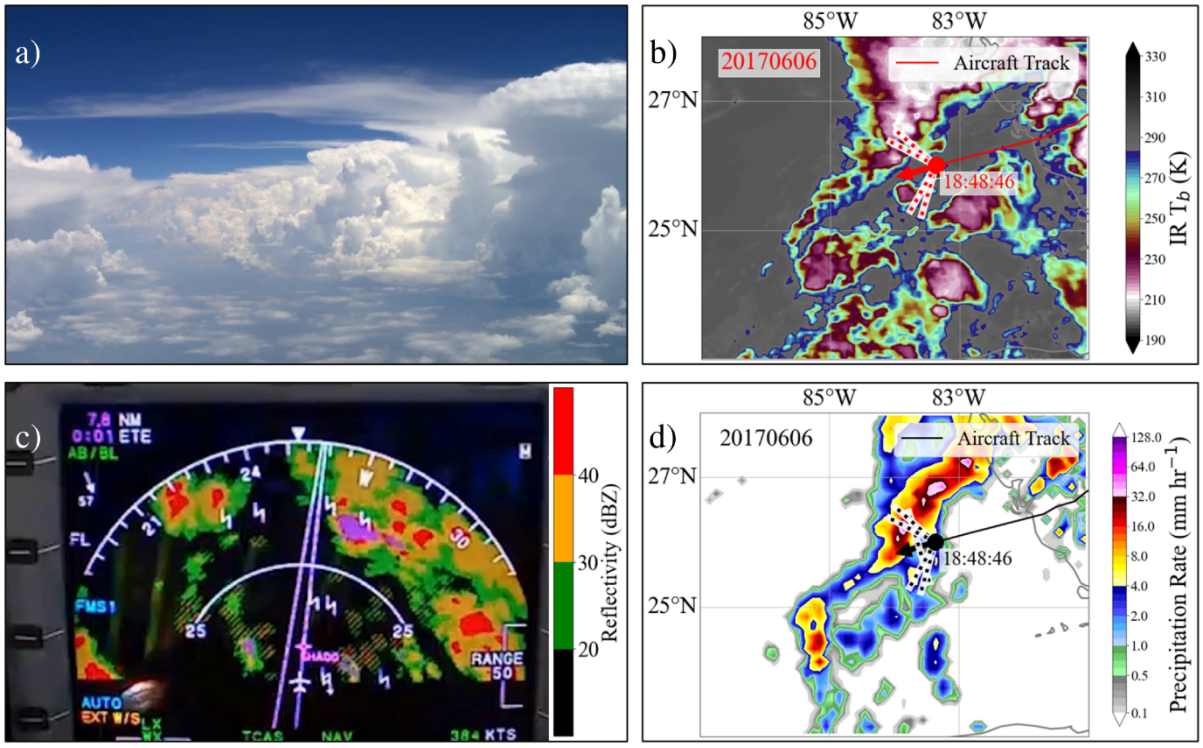

Fig. 4. Images from the CPEX mission on June 6th 2017 around 18:48 UTC: (a) the DC-8 aircraft's forward camera, (b) Merged-IR data at 19:00 UTC, (c) the DC-8 aircraft pilot's radar with range circles at 25 and 50 knots. and (d) IMERG precipitation for the half-hour period 18:30-19:00 UTC. Infrared and IMERG images are overlaid with the DC-8 track (red and black line, respectively). The red/black dot represents the DC-8 aircraft location, the arrow points in the direction of the aircraft heading, and the two dotted lines represent the minimum (88°) and maximum (115°) horizontal field of view (FOV) for the forward camera.

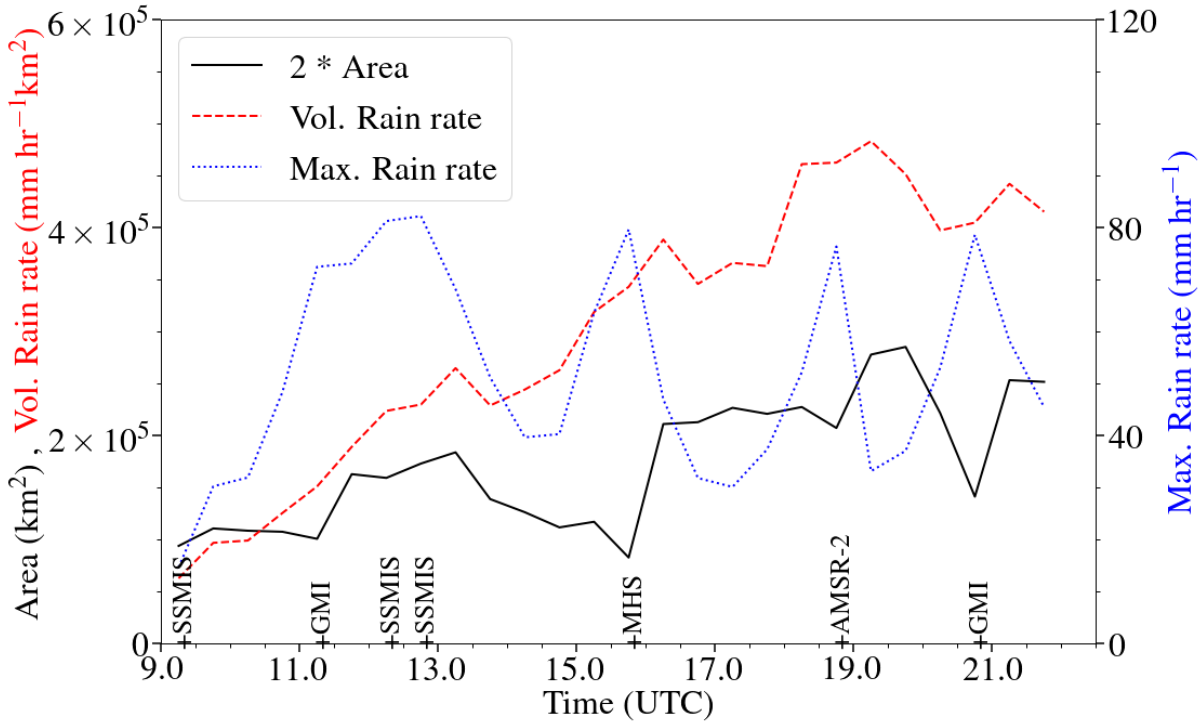

Fig. 5. Time series of the IMERG precipitation area, rain volume, and maximum rain rate of the MCS observed on June 6th 2017, CPEX mission. Since the volumetric rain rate and precipitation area share the same y-axis, the precipitation area is multiplied by a factor of two to make its variations more visible. PMW sensor names are annotated on the x-axis at their respective half-hour overpass interval.

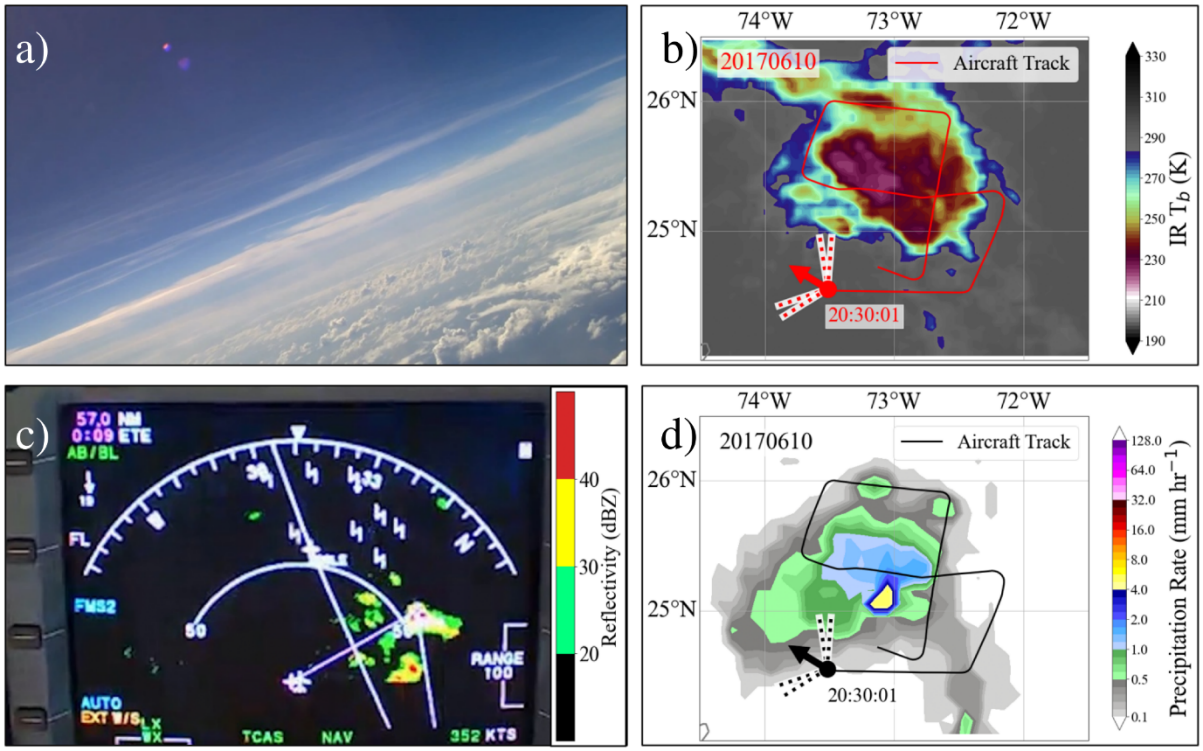

785

786 Fig. 6. Images from the CPEX mission on June 10th 2017 around 20:30 UTC: (a) the DC-8 aircraft's forward
787 camera, (b) Merged-IR data at 18:30 UTC, (c) the DC-8 aircraft pilot's radar with range circles at 50 and 100
788 knots. Note that the color bar in Fig. 6c differs from Fig. 4c due to different ambient lighting when recording
789 them, and (d) IMERG precipitation for the half-hour period 20:30-21:00 UTC. Infrared and IMERG images are
790 overlaid with the DC-8 track (red and black line, respectively). The red/black dot represents the DC-8 aircraft
791 location, the arrow points in the direction of the aircraft heading, and the two dotted lines represent the minimum
792 (100°) and maximum (126°) diagonal field of view (FOV) for the forward camera.

793

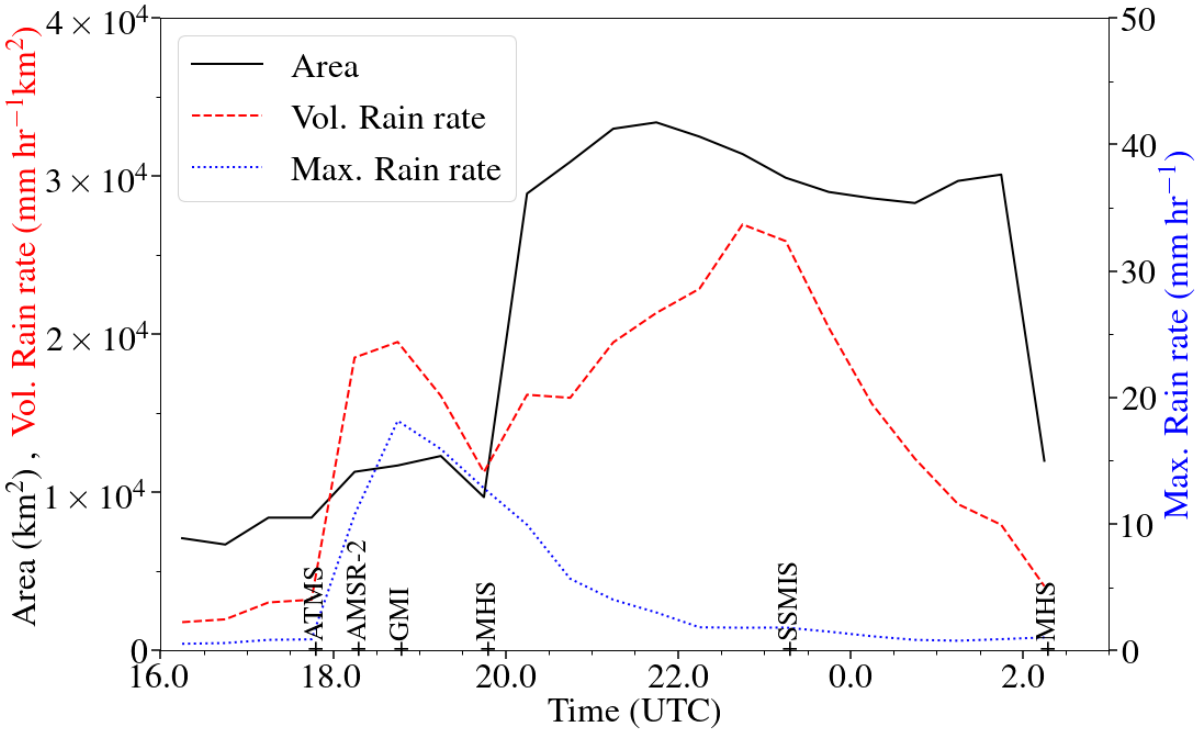

Fig. 7. Time series of the IMERG precipitation area, rain volume, and maximum rain rate of the MCS observed on June 10th 2017, CPEX mission. PMW sensor names are annotated on the x-axis at their respective half-hour overpass interval.

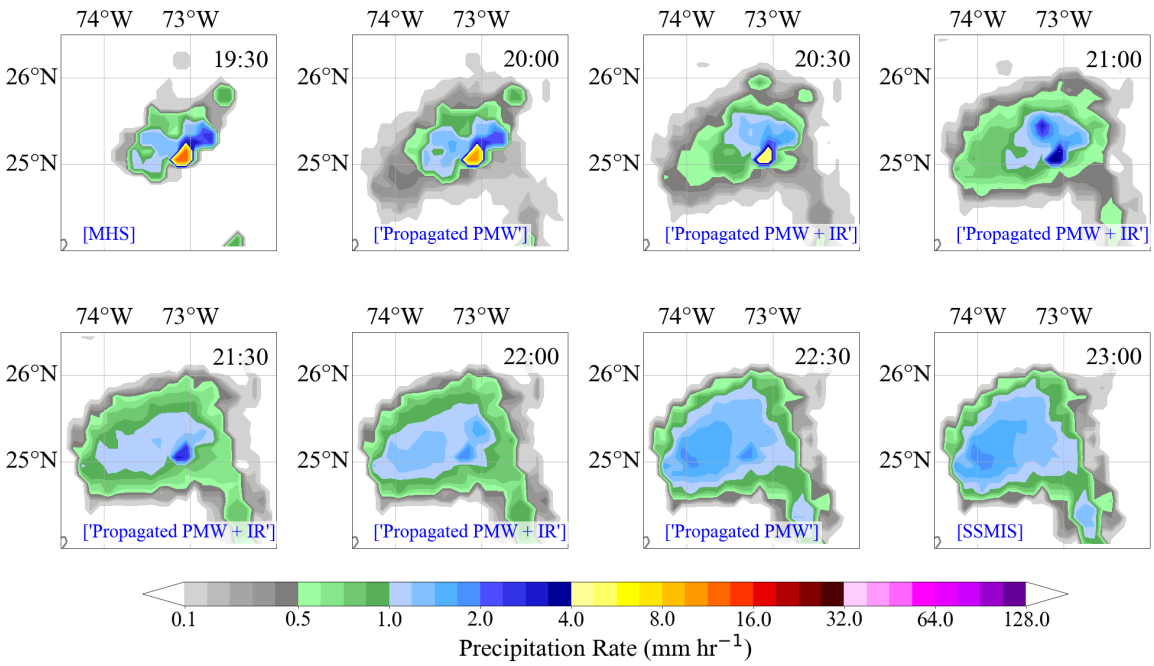

804

805 Fig. 8. IMERG precipitation from 19:30 through 23:00 UTC for the MCS observed on June 10th 2017. There were
806 PMW overpasses during half-hours starting at 19:30 and 23:00 UTC. IMERG precipitation during intermediate
807 intervals is estimated by the morphing algorithm using the Kalman weighted average of propagated PMW and IR
808 precipitation.

809

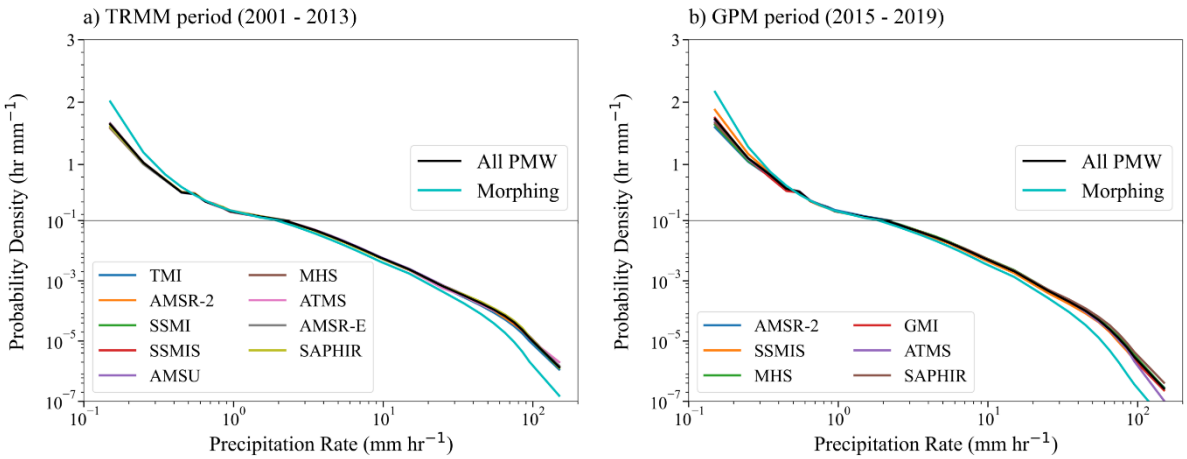

Fig. 9. The precipitation rate distribution of estimates from the GPROF algorithm (for various PMW sensors), and the morphing algorithm. The y-axis is linear for the upper half, and it is logarithmic for the lower half to make differences more discernable at the tails of the distribution.

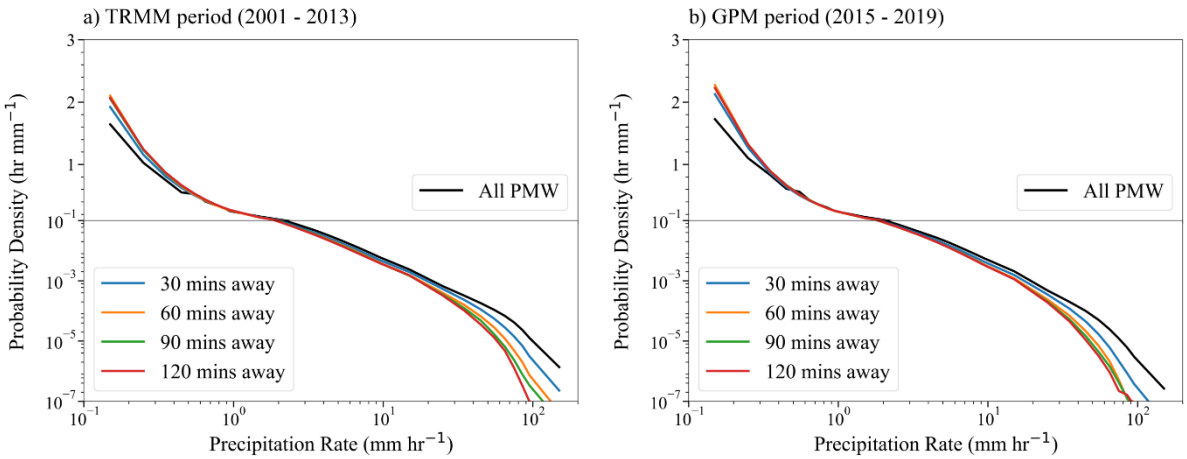

816

817 Fig. 10. The precipitation rate distribution for estimates from the morphing algorithm, as a function of time away
818 from the PMW observation. The y axis is linear for the upper half, and it is logarithmic for the lower half to make
819 differences more discernable at the tails of the distribution.

820
821

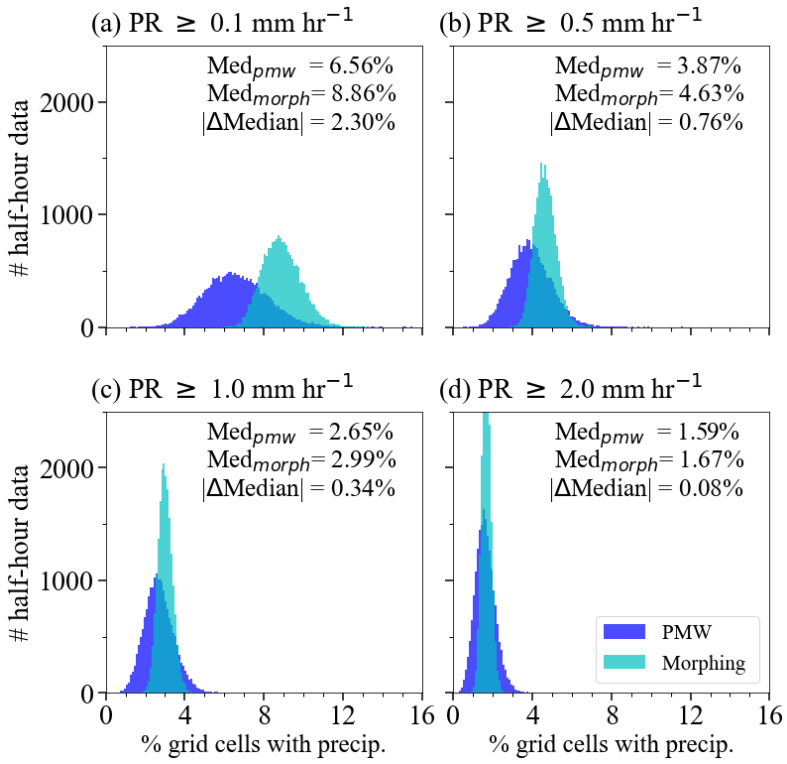

822

823 Fig. 11 Variability in tropical precipitation occurrence for PMW and morphing estimates, expressed as "% of grid
824 cells with precipitation", from 19,000 half-hour data randomly chosen from 2001 to 2019. Sub-plots show the
825 change in precipitation occurrence for precipitation rate (PR) thresholds of a) 0.1, b) 0.5, c) 1.0, and d) 2.0 mm
826 hr^{-1}.

827